Astronomy & Astrophysics manuscript no. i16293cyanopolyynes-2016Ago09
August 9, 2016

The history of the solar type protostar IRAS16293–2422 as told by the cyanopolyynes

A. A. Jaber[1,2,3], C. Ceccarelli[1,2,], C. Kahane[1,2], S. Viti[4], N. Balucani[5,1], E. Caux[6,7], B. Lefloch[1,2], F. Lique[8], E. Mendoza[9], D. Quenard[6,7], and L. Wiesenfeld[1,2]

[1] Univ. Grenoble Alpes, IPAG, F-38000 Grenoble, France e-mail: ali.al-edhari@univ-grenoble-alpes.fr
[2] CNRS, IPAG, F-38000 Grenoble, France
[3] University of AL-Muthanna, College of Science, Physics Department, AL-Muthanna, Iraq
[4] University College London, Gower Street, London, UK
[5] Dipartimento di Chimica, Biologia e Biotecnologie, Perugia, Italy
[6] Université de Toulouse, UPS-OMP, IRAP, Toulouse,France
[7] CNRS, IRAP, 9 Av. Colonel Roche, BP 44346, 31028 Toulouse Cedex 4, France
[8] LOMC – UMR 6294, CNRS-Université du Havre, 25 rue Philippe Lebon, BP 1123, 76063 Le Havre, France
[9] Instituto de Astronomia, Geofísica e Ciencias Atmosféricas, Universidade de Sao Paulo, Sao Paulo 05508-090, SP, Brazil

Received ; accepted

ABSTRACT

Context. Cyanopolyynes are chains of carbon atoms with an atom of hydrogen and CN group on either side. They are detected almost everywhere in the ISM, as well as in comets. In the past, they have been used to constrain the age of some molecular clouds, since their abundance is predicted to be a strong function of time. Finally, cyanopolyynes can potentially contain a large fraction of molecular carbon.

Aims. We present an extensive study of the cyanopolyynes distribution in the solar type protostar IRAS16293-2422. The goals are: (i) to obtain a census of the cyanopolyynes present in this source, as well as of their isotopologues; (ii) to derive how their abundance varies across the protostar envelope; (iii) to obtain constraints on the history of IRAS16293-2422 by comparing the observations with the predictions of a chemical model.

Methods. We analyse the data from the IRAM-30m unbiased millimeter and submillimeter spectral survey towards IRAS16293-2422 named TIMASSS. The derived Spectral Line Energy Distribution (SLED) of each detected cyanopolyyne is compared with the predictions from the radiative transfer code GRAPES (GRenoble Analysis of Protostellar Envelope Spectra) to derive the cyanopolyynes abundance across the envelope of IRAS16293-2422. Finally, the derived abundances are compared with the predictions of the chemical model UCL_CHEM.

Results. We detect several lines from cyanoacetylene (HC_3N) and cyanodiacetylene (HC_5N), and report the first detection of deuterated cyanoacetylene, DC_3N, in a solar type protostar. We found that the HC_3N abundance is roughly constant ($\sim 1.3\times10^{-11}$) in the outer cold envelope of IRAS16293-2422 and it increases by about a factor 100 in the inner region where the dust temperature exceeds 80 K, namely when the "volcano" ice desorption is predicted to occur. The HC_5N has an abundance similar to HC_3N in the outer envelope and about a factor of ten lower in the inner region. The comparison with the chemical model predictions provides constraints on the oxygen and carbon gaseous abundance in the outer envelope and, most importantly, on the age of the source. The HC_3N abundance derived in the inner region, and where the increase occurs, also provide strong constraints on the time taken for the dust to warm up to 80 K, which is has to be less than $\sim 10^3 - 10^4$ yr. Finally, the cyanoacetylene deuteration is about 50% in the outer envelope and ~ 5% in the warm inner region. The relatively low deuteration in the warm region suggests that we are witnessing a fossil of the HC_3N abundantly formed in the tenuous phase of the pre-collapse and then frozen into the grain mantles at a later phase.

Conclusions. The accurate analysis of the cyanopolyynes in IRAS16293-2422 unveils a precious part of its past story. It tells us that IRAS16293-2422 underwent a relatively fast ($\leq 10^5$ yr) collapse and a very fast ($\leq 10^3 - 10^4$ yr) warming up of the cold material to 80 K.

Key words. Astrochemistry – ISM: clouds – ISM: abundances – ISM: molecules – ISM:

1. Introduction

Cyanopolyynes, H-C_{2n}-CN, are linear chains of $2n+1$ carbon bonded at the two extremities with a hydrogen and a CN group atom, respectively. They seem to be ubiquitous in the ISM, as they have been detected in various environments, from molecular clouds to late type carbon rich AGB stars. The detection of the largest cyanopolyyne, $HC_{11}N$, has been reported in the C-rich AGB star IRC+10216 (Cernicharo & Guelin 1996) and the molecular cloud TMC-1 (Bell et al. 1997), which shows an anomalously large abundance of cyanopolyynes with respect to other molecular clouds. Curiously enough, in star forming regions, only relatively short chains have been reported in the literature so far, up to HC_7N, in dense cold cores and WCCC (Warm Carbon Chain Chemistry) sources (e.g. Sakai et al.

2008; Cordiner et al. 2012; Friesen et al. 2013). For many years, cyanopolyynes have been suspected to be possible steps towards the formation of simple amino acids (e.g. Brack 1998). More recently, the rich N-chemistry leading to large cyanopolyynes chains observed in Titan has renewed the interest towards this family of molecules, as Titan is claimed to be a possible analogue of the early Earth (Lunine 2009). An important property of cyanopolyynes, and particularly relevant for astrobiological purposes, is that they are more stable and robust against the harsh interstellar environment compared to their monomer, and hence they may better resist the exposure to UV and cosmic rays (Clarke & Ferris 1995). Very recent observations towards the comet 67P/Churyumov-Gerasimenko by Rosetta seem to support the idea that cyanides polymers, and, by analogy, cyanopolyynes, are abundant on the comet's surface (Goesmann et al. 2015).

Whatever the role of cyanopolyynes in prebiotic chemistry, when trapped in interstellar ices, they for sure can carry large quantities of carbon atoms. It is, therefore, of interest to understand in detail their formation, carbon chain accretion and evolution in Solar-like star forming regions. The goal of this article is to provide the first census of cyanopolyynes in a Solar-like protostar. To this end, we used the 3-1mm unbiased spectral survey TIMASSS (§3) towards the well studied protostar IRAS16293-2422 (§2), to derive the abundance across the envelope and hot corino for HC_3N, HC_5N and their respective isotopologues (§4). The measured abundance profiles provide us with constraints on the formation routes of these species (§5). A final section (§6) discusses the implications of the analysis.

2. Source description

IRAS16293-2422 (hereinafter IRAS16293) is a solar type Class 0 protostar in the ρ Ophiuchus star forming region, at a distance of 120 pc (Loinard et al. 2008). It has a bolometric luminosity of 22 $L_\odot$ (Crimier et al. 2010). Given its proximity and brightness, it has been the target of numerous studies that have reconstructed its physical and chemical structure. Briefly, IRAS16293 has a large envelope that extends up to ∼6000 AU and that surrounds two sources, named I16293-A and I16293-B in the literature, separated by $\sim 5''$ (∼600 AU; Wootten (1989); Mundy et al. (1992)). I16293-A sizes are $\sim 1''$, whereas I16293-B is unresolved at a scale of $\sim 0.4''$ (Zapata et al. 2013). I16293-A itself is composed of at least two sources, each one emitting a molecular outflow (Mizuno et al. 1990; Loinard et al. 2013). I16293-B possesses a very compact outflow (Loinard et al. 2013) and is surrounded by infalling gas (Pineda et al. 2012; Zapata et al. 2013). From a chemical point of view, IRAS16293 can be considered as composed of an outer envelope, characterised by low molecular abundances, and a hot corino, where the abundance of many molecules increases by orders of magnitude (e.g. Ceccarelli et al. 2000; Schöier et al. 2002; Cazaux et al. 2003; Jaber et al. 2014). The transition between the two regions occurs at ∼100 K, the sublimation temperature of the icy grain mantles.

3. The data set

3.1. Observations

We used data from The IRAS16293 Millimeter And Submillimeter Spectral Survey (TIMASSS; Caux et al. (2011)). Briefly, the survey covers the 80-280 GHz frequency interval and it has been obtained at the IRAM-30m, during the period January 2004 to August 2006 ($\sim$ 200 hr). Details on the data reduction and calibration can be found in Caux et al. (2011). We recall here the major features, relevant for this work. The telescope beam depends on the frequency and varies between 9" and 30". The spectral resolution varies between 0.3 and 1.25 MHz, corresponding to velocity resolutions between 0.51 and 2.25 km/s. The achieved rms ranges from 4 to 17 mK. Note that it is given in a 1.5 km/s bin for observations taken with a velocity resolution ≤1.5km/s, and in the resolution bin for larger velocity resolutions. The observations are centered on I16293-B at $\alpha(2000.0) = 16^h\ 32^m\ 22^s.6$ and $\delta(2000.0)$= -24° 28′ 33″. Note that the I16293-A and I16293-B components are both inside the beam of the observations at all frequencies.

3.2. Species identification

We searched for the lines of the cyanopolyynes and their isotopologues using the spectroscopic databases JPL(Jet Propulsion Laboratory) (Pickett et al. 1998) and CDMS (Cologne Database for Molecular Spectroscopy) (Müller et al. 2005), and the package CASSIS (Centre d'Analyse Scientifique de Spectres Instrumentaux et Synthétiques) (*http://cassis.irap.omp.eu*) for gaussian fitting to the lines. For the line identification we adopted the following criteria:

1. The line is detected with more than 3σ in the integrated line intensity.
2. The line is not blended with other molecular lines.
3. The line intensity is "compatible" with the Spectral Line Energy Distribution (SLED): since cyanopolyyynes are linear molecules, their SLED is a smooth curve, so that lines having intensities that are out of the SLED defined by the majority of the lines are discarded, as shown in Fig. A.1.
4. The line FWHM is similar to that of the other cyanopolyynes lines with a similar upper level energy. In practice, *a posteriori* the FWHM is about 2 km/s for lines with J≤12, and increases to 6–7 for J=22–30 lines.
5. The line rest velocity V_{LRS} does not differ by more than 0.5 km/s from the V_{LRS} of the other cyanopolyynes lines.

Following the first two criteria leads to the detection of 18 lines of HC_3N (from J=9-8 to J=30-29), 9 lines of HC_5N (from J=31-30 to J=39-38) and the detection of 6 lines of DC_3N (from J=10-9 to J=17-16). The full list of detected lines with their spectroscopic parameters is reported in Table 1. All the spectra are shown in Fig. 1, 2 and 3 for HC_3N, HC_5N and DC_3N, respectively. We did not detect any line from the ^{13}C isotopologues of HC_3N.

The application of the remaining three criteria leads us to discard four HC_3N lines (at 109.173, 245.606, 254.699 and 263.792 GHz), which suffer of calibration problems (Caux et al. 2011) and/or blending with unidentified species (see Fig. A.1). Similarly, one HC_5N line (at 95.850 GHz) was discarded, because of its abnormal value for the intensity, FWHM and velocity compared to the rest of the

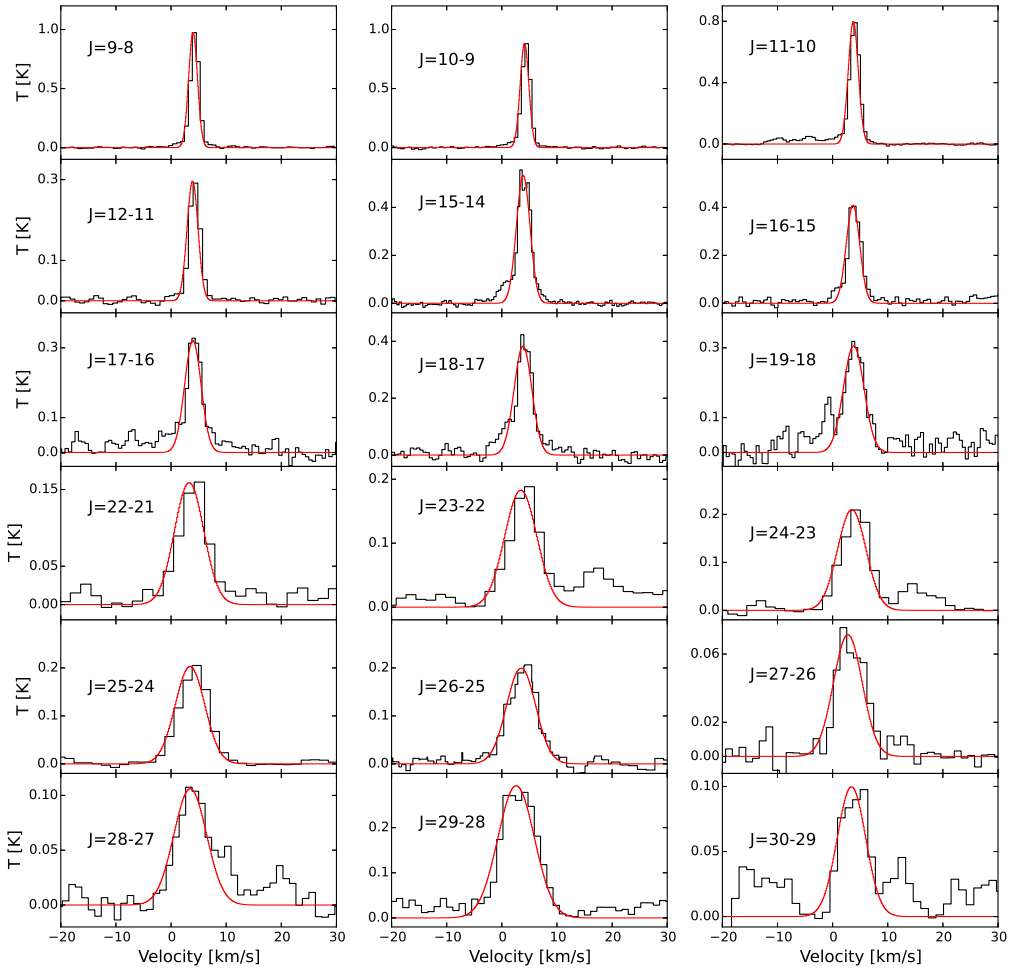

Fig. 1. Observed spectra of the detected lines of HC_3N. The red curves show the Gaussian fits. The temperature is a main beam antenna temperature.

lines (see Tab. 1). Finally, one DC_3N (at 135.083 GHz) is considered as tentatively detected.

In summary, we clearly detected HC_3N, HC_5N and DC_3N, for which 14, 8 and 6 lines have been identified following the five criteria above. We did not detect any ^{13}C isotopologue of HC_3N, nor cyanopolyynes larger than HC_5N.

4. Line modeling

4.1. Model description

As in our previous work (Jaber et al. 2014, hereinafter Paper I), we used the package GRAPES (GRenoble Analysis of Protostellar Envelope Spectra), based on the code described in Ceccarelli et al. (1996, 2003), to interpret the Spectral Line Energy Distribution (SLED) of the detected cyanopolyynes. Briefly, GRAPES computes the SLED from a spherical infalling envelope for a given density and temperature structure. The code uses the beta escape formalism to locally solve the level population statistical equilibrium equations and consistently computes each line optical depth by integrating it over the solid angle at each point of the envelope. The predicted line flux is then integrated over the whole envelope after convolution with the telescope beam. The abundance X (with respect to H_2) of the considered species is assumed to vary as a function of the radius with a power law α in the cold part of the envelope, and as a "jump" to a new abundance in the warm part, corresponding to the sublimation of ices (see, e.g. Caselli & Ceccarelli (2012)). The transition between the two regions is set by the dust temperature, to simulate the sublimation of the ice mantles, and occurs at T_{jump}.

The abundance is, therefore, given by:

$$\begin{aligned} X(r) &= X_{out}\left(\frac{r}{R_{max}}\right)^{\alpha} \qquad T_{dust} \leq T_{jump} \\ X(r) &= X_{in} \qquad\qquad\qquad\quad T_{dust} > T_{jump} \end{aligned} \tag{1}$$

where R_{max} represents the largest radius of the envelope. In the present study, we use the physical structure of the IRAS16293 envelope derived by Crimier et al. (2010), where the maximum radius is 1×10^{17} cm.

We carried out non-LTE calculations for all species. We have used the collisional coefficients for HC_3N computed by Faure et al. (2016). For DC_3N collisional coefficients, we have assumed the same as those of HC_3N. Finally, the collisional coefficients for HC_5N have been computed by Lique et. al. (in preparation). Briefly, HC_5N rate coefficients were extrapolated from HCN (Ben Abdallah et al. 2012) and HC_3N (Wernli et al. 2007) considering

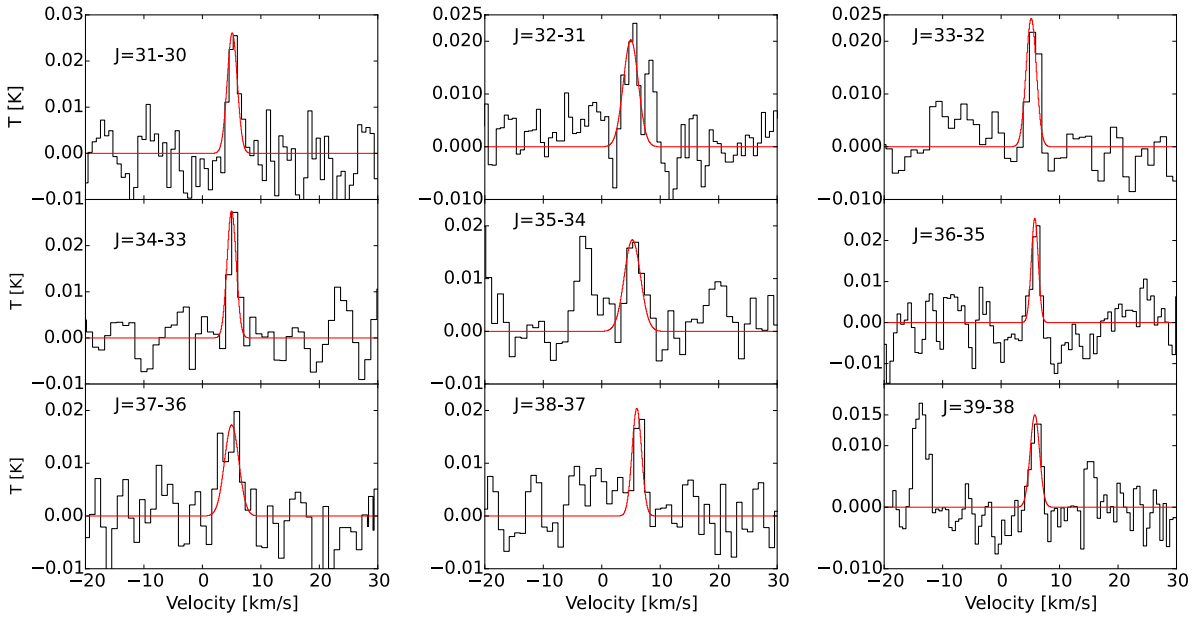

Fig. 2. Observed spectra of the detected lines of HC_5N. The red curves show the Gaussian fits. The temperature is a main beam antenna temperature.

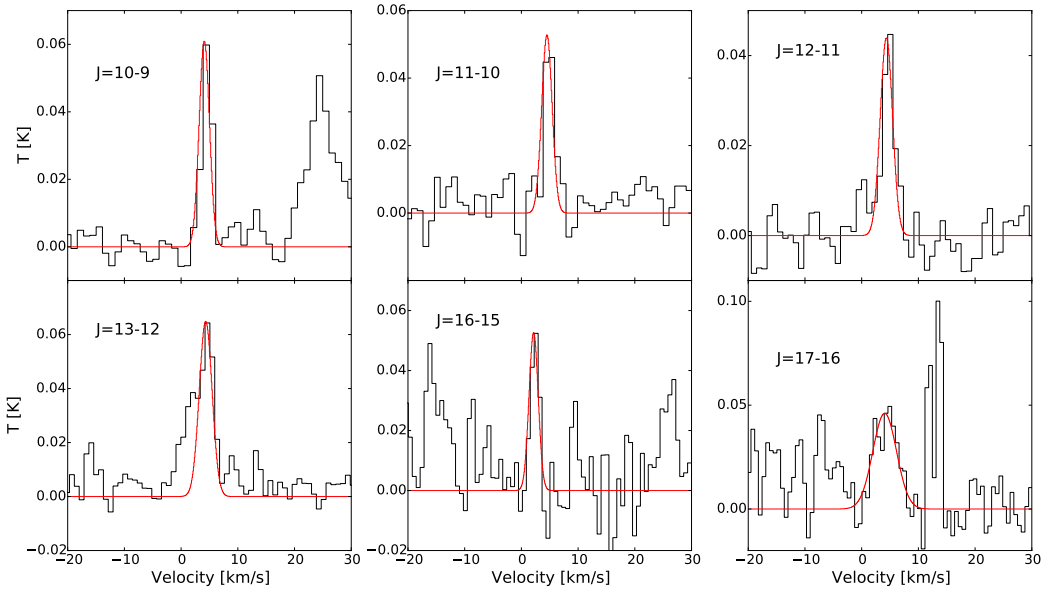

Fig. 3. Observed spectra of the detected lines of DC_3N. The red curves show the Gaussian fits. The temperature is a main beam antenna temperature.

that the cyanopolyynes rate coefficients are proportional to the size of the molecules as first suggested by Snell et al. (1981). However, in order to improve the accuracy of the estimation, we consider scaling factors depending also on the transition and the temperature. Hence, the ratio of HC_3N over HCN rate coefficients was also used to evaluate the HC_5N ones as follow :

$$k_{HC_5N}(T) = k_{HC_3N}(T) * [\frac{1}{2} + \frac{1}{2}\frac{k_{HC_3N}(T)}{k_{HCN}(T)}] \quad (2)$$

Finally, note that the disadvantage of GRAPES, namely its incapacity to compute the emission separately for the two sources I16293-A and I16293-B (Jaber et al. 2014), can be neglected here because previous interferometric observations by Chandler et al. (2005) and Jørgensen et al. (2011) have demonstrated that the cyanopolyynes line emission arises from source I16293-A, as also found by the analysis by Caux et al. (2011).

We run large grids of models varying the four parameters, X_{in}, X_{out}, α and T_{jump}, and found the best fit to the observed fluxes. In general, we explored the X_{in}–X_{out} parameter space by running 10x10 and 20x20 grids for α equal to -1, 0, +1 and +2, and T_{jump} from 10 to 200 K by steps of 10 K. Note that we first started with a 3 or 4 orders of mag-

Table 1. Parameters of the detected cyanopolyynes lines.

Transition	Frequency[c] [MHz]	E_{up} [K]	V_{LSR} [km/s]	FWHM [km/s]	Int. [K.km/s]	beam ["]
			HC_3N			
9-8[a]	81881.4	19.6	3.9(0.6)	2.2(0.6)	2.5(0.4)	29.5
10-9[a]	90979.0	24.0	3.9(0.5)	2.1(0.5)	2.3(0.4)	26.5
11-10[a]	100076.3	28.8	3.9(0.4)	2.2(0.4)	2.2(0.3)	24.1
12-11[b]	109173.6	34.1	3.9(0.4)	2.3(0.4)	0.9(0.1)	22.1
15-14	136464.4	52.4	3.9(0.3)	2.9(0.3)	2.1(0.3)	17.7
16-15	145560.9	59.4	3.6(0.2)	2.8(0.3)	1.7(0.3)	16.6
17-16	154657.2	66.8	3.9(0.2)	3.1(0.3)	1.6(0.2)	15.6
18-17	163753.3	74.7	3.9(0.2)	3.5(0.3)	2.1(0.3)	14.7
19-18	172849.3	82.9	3.8(0.2)	4.4(0.2)	2.1(0.3)	14.0
22-21	200135.3	110.5	3.2(0.5)	6.1(0.7)	1.6(0.2)	12.1
23-22	209230.2	120.5	3.4(0.5)	6.5(0.6)	2.1(0.3)	11.5
24-23	218324.7	131.0	3.4(0.5)	6.1(0.5)	2.2(0.3)	11.1
25-24	227418.9	141.9	3.4(0.4)	6.3(0.5)	2.3(0.3)	10.6
26-25	236512.7	153.2	3.4(0.4)	6.2(0.5)	2.3(0.3)	10.2
27-26[b]	245606.3	165.0	2.7(0.5)	6.1(0.7)	0.8(0.1)	9.8
28-27[b]	254699.5	177.2	3.4(0.4)	7.0(0.4)	1.5(0.2)	9.5
29-28[b]	263792.3	189.9	2.5(0.3)	7.8(0.5)	4.7(0.7)	9.1
30-29	272884.7	203.0	3.4(0.6)	6.6(1.0)	1.4(0.2)	8.8
			HC_5N[c]			
31-30	82539.0	63.4	3.7(0.7)	1.7(0.7)	0.08(0.01)	29.2
32-31	85201.3	67.5	3.9(0.6)	2.6(0.7)	0.07(0.01)	28.3
33-32	87863.6	71.7	4.0(0.6)	2.0(0.6)	0.06(0.01)	27.5
34-33	90525.9	76.0	3.9(0.6)	1.8(0.6)	0.06(0.01)	26.7
35-34	93188.1	80.5	3.9(0.5)	2.7(0.5)	0.06(0.01)	25.9
36-35[b]	95850.3	85.1	4.5(0.6)	1.4(0.7)	0.04(0.01)	25.2
37-36	98512.5	89.8	3.8(0.6)	2.7(1.2)	0.06(0.01)	24.5
38-37	101174.7	94.7	4.6(0.5)	1.8(0.6)	0.05(0.01)	23.9
39-38	103836.8	99.6	4.3(0.5)	1.9(0.5)	0.03(0.01)	23.2
			DC_3N			
10-9	84429.8	22.3	3.9(0.6)	2.1(0.6)	0.17(0.06)	28.6
11-10	92872.4	26.7	4.4(0.5)	2.1(0.7)	0.14(0.05)	26.0
12-11	101314.8	31.6	4.3(0.4)	2.6(0.5)	0.15(0.05)	23.8
13-12	109757.1	36.9	4.1(0.4)	2.7(0.5)	0.26(0.10)	22.1
16-15[d]	135083.1	55.1	2.1(0.3)	1.7(0.4)	0.13(0.05)	17.7
17-16	143524.8	62.0	4.3(0.2)	3.8(0.4)	0.27(0.10)	16.6

The first three columns report the transition, frequency and upper energy level (E_{up}). The next three columns report the result of the gaussian fitting: V_{LSR} velocity, full width at half maximum (FWHM) and velocity-integrated line intensity (Int.). The last column reports the telescope beam at the frequency of the line.
[a]: Discarded line because likely contaminated by the molecular cloud (see text, §4.2).
[b]: Discarded line because it does not satisfy criteria 3 to 5 of §3.2.
[c] The HC_3N and DC_3N line frequencies are the same in the CDMS and JPL database. On the contrary, the JPL HC_5N line frequencies are systematically overestimated with respect to those of CDMS, giving V_{LSR} shifted by ~ 1 km/s with respect to the V_{LSR} derived for the HC_3N and DC_3N lines. Thus, we used the HC_5N line frequencies from the CDMS database.
[d] We consider this a tentative detected line.

nitude range in X_{in} and X_{out} to find a first approximate solution and then we fine-tuned the grid around it.

4.2. Results

4.2.1. HC_3N

The HC_3N SLED has been analysed in two steps, as follows. *Step 1*: We first run a grid of models varying T_{jump}, X_{in} and X_{out} with α=0. The best fit for this first step is obtained with T_{jump}=80 K, $X_{in} = 3.6 \times 10^{-10}$, and $X_{out} = 6.0 \times 10^{-11}$. However, the fit is not very good (reduced χ^2=1.7). We plotted for each line the predicted velocity-integrated flux emitted from a shell at a radius r (namely $dF/dr * r$) as a function of the radius, as shown in Fig. A.2. For the three lines with the lowest J (from J=9 to 11) the predicted shell-flux increases with the radius and abruptly stops at the maximum radius of the envelope. Therefore, these three lines are very likely contaminated by the molecular cloud, which could explain the bad χ^2. In the second modeling step, thus, we excluded these lines and repeated the modeling, as described below.

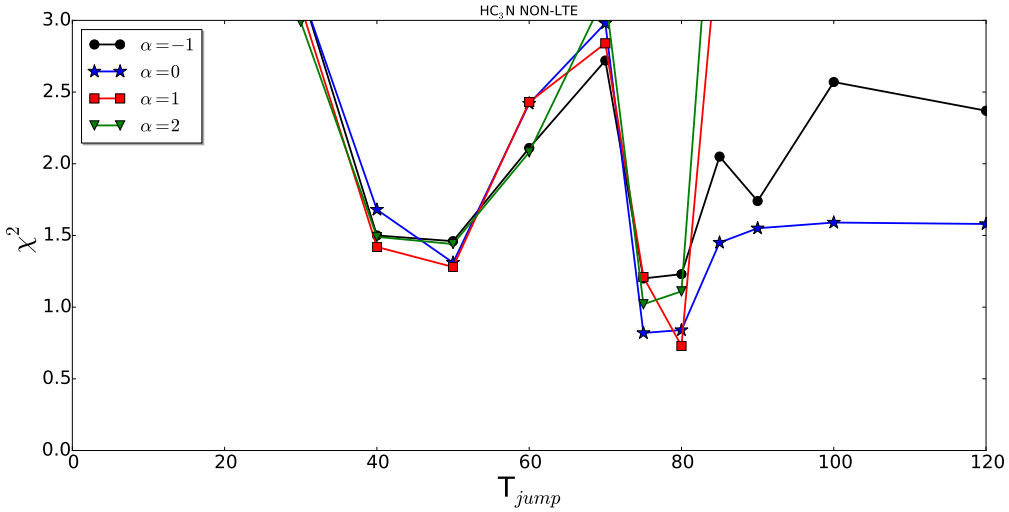

Fig. 4. Results of the HC_3N modeling. The best reduced χ^2 optimised with respect to X_{in} and X_{out} as a function of T_{jump}.

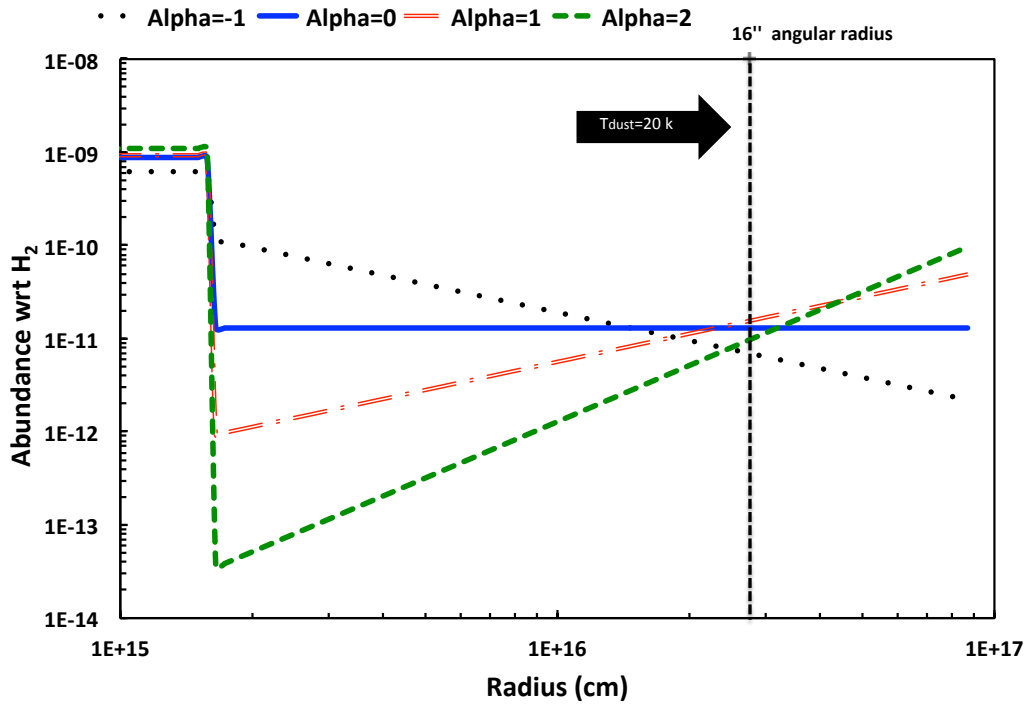

Fig. 5. Abundance profiles of the four HC_3N best fit models of Tab. 2.

Step 2: We run a grid of models as in step 1 and, indeed, found a better χ^2 (0.8). We, therefore, extended the analysis varying the α parameter between -1 and +2, together with the other three parameters T_{jump}, X_{in} and X_{out}. The results are reported in Fig. 4 and Table 2. Note that, in Table 2, we also report the values of the abundance of the envelope, X_{T20}, at a radius equal to the angular size of the beam with the lowest frequencies, namely 29".5 in diameter. At that radius, which is 2.75×10^{16} cm (around 1800 AU), the envelope dust temperature is 20 K.

Fig. 4 shows the χ^2 obtained for each value of α, minimised with respect to X_{in} and X_{out}, as a function of T_{jump}. A χ^2 less than unity is obtained with T_{jump} equal to 80 K and α equal to 0 and 1 (Table 2). Fig. 5 shows the abundance profiles of HC_3N as predicted by the best fit models. Note that the four models have the same T_{jump} (80 K), and the same X_{in} (9×10^{-10}) and X_{T20} at 20 K ($\sim 1\times10^{-11}$), within a factor 2. Therefore, the determination of T_{jump}, X_{in} and X_{out} at 20 K is very robust and depends very little on the assumption of the HC_3N abundance distribution.

Given the similarity of our results regardless of α, in the following, we will only consider the case of α=0. Fig. A.3 shows the χ^2 contour plots as a function of the inner X_{in} and outer X_{out} with T_{jump}=80 K. Fig. A.4 reports the ratio of the observed over predicted line fluxes as a function of the upper level energy of the transition, to show the goodness

Table 2. Results of the HC_3N modeling. Values of the best fit using four different values of α.

Model No.	α	T_{jump} [K]	X_{in} [10^{-10}]	X_{out} [10^{-10}]	X_{T20} [10^{-10}]	X_{in}/X_{out}	X_{in}/X_{T20}	χ^2
Model 1	-1	80±5	6±1	$0.020^{+0.009}_{-0.001}$	$0.07^{+0.03}_{-0.01}$	300^{+70}_{-130}	90^{+30}_{-40}	1.2
Model 2	0	80±5	9±1	$0.13^{+0.03}_{-0.04}$	$0.13^{+0.03}_{-0.04}$	90^{+20}_{-40}	90^{+20}_{-40}	0.8
Model 3	1	80±5	9±1	$0.5^{+0.1}_{-0.2}$	0.2±0.1	18^{+15}_{-5}	45^{+55}_{-20}	0.7
Model 4	2	80±5	11±1	$1.0^{+0.1}_{-0.4}$	$0.10^{+0.01}_{-0.04}$	11^{+9}_{-2}	110^{+90}_{-20}	1.1

of the best fit model. Finally, Fig. A.5 shows the predicted shell-flux as a function of the radius for a sample of lines. As a final remark, we note that we also run LTE models and obtained approximately the same results.

4.2.2. HC_5N

Having less lines, we decided to assume that HC_5N follows the spatial distribution of HC_3N and run a grid of models with α=0, and T=80 K and X_{in} and X_{out} as free parameters. The X_{in}–X_{out} χ^2 surface is shown in Fig. A.3 and the ratio between the observed and best fit predicted intensities is shown in Fig. A.4. Table 3 summarises the best fit values. We only obtained an upper limit to the X_{in} abundance, $\leq 8\times10^{-11}$, while the X_{out} abundance is $\sim 1\times10^{-11}$. When compared to HC_3N, the HC_5N abundance is, therefore, more than ten times lower in the hot corino region, while it is the same in the outer cold envelope.

4.2.3. DC_3N

Following the discussion on the HC_3N line analysis, we did not consider the three DC_3N lines with the lowest upper level energy, as they are likely contaminated by the molecular cloud.

For the remaining three lines, we adopted the same strategy as for HC_5N for the SLED analysis, namely we adopted α=0, and T=80 K and varied X_{in} and X_{out}. The results are shown in Figs. A.3 and A.4, and summarised in Table 3. We obtained an upper limit of X_{in}, $\leq 4\times10^{-11}$, while X_{out} is $\sim 5\times10^{-12}$. This implies a deuteration ratio of $\sim$ 5% and 50% in the hot corino and cold envelope, respectively.

4.2.4. Undetected species and final remarks on the observations

As mentioned earlier, we do not detect larger cyanopolyynes nor ^{13}C isotopologues. For the undetected species we derived the upper limits to the abundance by assuming that the non-detected emission arises in the hot corino (with a temperature of 80 K, diameter = 2″, $N(H_2) = 1.5\times10^{23}$ cm^{-2}, line FWHM = 6 km/s), and cold envelope (with a temperature of 20 K, diameter = 30", $N(H_2) = 3.5\times10^{22}$ cm^{-2}, line FWHM = 3 km/s), respectively. The results are listed in Table 3.

From the HC_5N and DC_3N modeling, we conclude that the detected lines of both species are dominated by the emission from the cold outer envelope, as we only obtain upper limits to their abundance in the warm inner region. This conclusion is coherent with the line widths reported in Table 1. Indeed, the HC_3N lines (see also Fig. A.1) show a clear separation between the low energy transitions, for which the FWHM is around 3 km/s, and the high energy ones, for which the FWHM is around 6 km/s or higher. This strongly suggests that the two sets of lines probe different regions. As the low energy lines correspond to E_{up} values lower than 80 K, a very natural explanation is that they are dominated by emission from the cold envelope, whereas the high energy lines ($E_{up} \geq 110$ K) are dominated by emission from the inner warm region. As the HC_5N and DC_3N lines present FWHM around 3 km/s, it is not surprising that our modeling concludes that they are dominated by emission from the cold envelope.

5. The chemical origin of HC_3N

As discussed in the Introduction, HC_3N is an ubiquitous molecule in the ISM. There are several routes by which a high HC_3N abundance may arise. Briefly, HC_3N can form via the following neutral-neutral reactions (e.g. Wakelam et al. 2015):

$C_2H_2 + CN \longrightarrow HC_3N + H$
$C_4H + N \longrightarrow HC_3N + C$
$C_3H_2 + N \longrightarrow HC_3N + H$
$C_2H + HNC \longrightarrow HC_3N + H$

in order of importance under the typical dense cloud conditions. Its main destruction channels are either via reactions with He^+ or reactions with atomic carbon. In dark clouds ($n_H \sim 10^4$–10^5 cm^{-3}), it is well known that HC_3N, together with other carbon chain moolecules, is abundant (e.g. Suzuki et al. (1992); Caselli et al. (1998)). Thus, based on its routes of formation and destruction, one would expect the HC_3N abundance to increase as a function of gas density, at least before freeze-out onto the dust grains takes over. Interestingly, however, the HC_3N abundance with respect to H_2 estimated in both the envelope and the hot corino of IRAS16293 is rather low ($\sim 10^{-11}$ and $\sim 10^{-9}$ respectively). In this section we, therefore, discuss the possible physical conditions that may lead to such low abundances of HC_3N.

5.1. Cold envelope

First of all, we investigate, qualitatively, what conditions in the cold envelope may lead to a fractional abundance of HC_3N as low as 10^{-11}. We would like to emphasise that this is not an easy task as very small changes in the main atomic elements (O, C, N) or molecular species (CO) can lead to very large changes in the abundances of tracers species. Hence, it is likely that small uncertainties in the initial elemental abundances of the cloud as well as its depletion history (which is dependent on the time the gas 'sits' at a particular gas density) can easily lead to differences in the abundances of species such as HC_3N of orders of magnitudes.

Table 3. Results of the analysis.

Species	Formula	X_{in} [10^{-10}]	X_{T20} [10^{-10}]	X/HC_3N [In]	X/HC_3N [T20]	χ^2
Detected cyanopolyynes						
Cyanoacetylene	HC_3N	9±1	$0.13^{+0.03}_{-0.04}$	1	1	0.8
Cyanodiacetylene	HC_5N	$\lesssim$0.8	0.110±0.005	$\lesssim$0.1	$0.8^{+0.2}_{-0.4}$	1.1
Deuterated Cyanoacetylene	DC_3N	$\lesssim$0.4	$0.049^{+0.002}_{-0.003}$	$\lesssim$0.04	$0.4^{+0.1}_{-0.2}$	1.9
Undetected cyanopolyynes						
Ethynylisocyanide	HCCNC	$\lesssim$ 7.5	$\lesssim$ 0.10			
3-Imino-1,2-propa-dienylidene	HNCCC	$\lesssim$ 1.2	$\lesssim$ 0.01			
Cyanoacetylene, ^{13}C	HCCC-13-N	$\lesssim$ 4.5	$\lesssim$ 0.10			
Cyanoacetylene, ^{13}C	HCC-13-CN	$\lesssim$ 4.5	$\lesssim$ 0.09			
Cyanoacetylene, ^{13}C	HC-13-CCN	$\lesssim$ 7.5	$\lesssim$ 0.15			
Cyanoacetylene, ^{15}N	HCCCN-15	$\lesssim$ 1.5	$\lesssim$ 0.15			
	DNCCC	$\lesssim$ 1.5	$\lesssim$ 0.04			
Cyanodiacetylene, ^{13}C	HCCCCC-13-N	$\lesssim$ 6.0	$\lesssim$ 0.60			
Cyanodiacetylene, ^{13}C	HCCCC-13-CN	$\lesssim$ 7.5	$\lesssim$ 0.60			
Cyanodiacetylene, ^{13}C	HCCC-13-CCN	$\lesssim$ 4.5	$\lesssim$ 0.45			
Cyanodiacetylene, ^{13}C	HCC-13-CCCN	$\lesssim$ 7.5	$\lesssim$ 0.75			
Cyanodiacetylene, ^{13}C	HC-13-CCCCN	$\lesssim$ 6.0	$\lesssim$ 0.60			
Cyanodiacetylene, ^{15}N	HCCCCCN-15	$\lesssim$ 7.5	$\lesssim$ 0.75			
Cyanodiacetylene, D	DCCCCCN	$\lesssim$ 7.5	$\lesssim$ 0.75			
Cyanohexatriyne	HC_7N	$\lesssim$ 15	$\lesssim$ 15			

Note: The first two columns report the species name and formula. Third and fourth columns report the values of the inner abundance X_{in} and the abundances at T_{dust}=20 K X_{T20}. Columns 5 and 6 report the values of the abundance ratios DC_3N/HC_3N and HC_5N/HC_3N, in the inner region and where T_{dust}=20 K respectively. Last column reports the χ^2 for the best fit of HC_5N and DC_3N (note that in this last case the χ^2 is not reduced). The top half table lists the detected species, the bottom half table the upper limits to the abundance of undetected cyanopolyynes (see text, § 4).

For our analysis, we make use of the time dependent chemical model UCL_CHEM (Viti et al. 2004). The code is used in its simplest form, namely we only included gas phase chemistry with no dynamics (the gas is always kept at a constant density and temperature). The gas phase chemical network is based on the UMIST database (McElroy et al. 2013) augmented with updates from the KIDA database as well as new rate coefficients for the HC_3N and HC_5N network as estimated by Loison et al. (2014). The chemical evolution is followed until chemical equilibrium is reached. In order to understand the chemical origin of the HC_3N abundance that we measured in the cold envelope of IRAS16293 ($\sim 10^{-11}$), we modeled a gas density of 2×10^6 cm^{-3} and a gas temperature of 20 K, which are the values inferred by Crimier et al. (2010) at a radius equivalent to the observations telescope beam (see §4.2.1).

We ran a small grid of models where we varied:

- the carbon and oxygen elemental abundances in the range of 0.3–1 and 1–3 $\times 10^{-4}$, respectively;
- the nitrogen elemental abundance: 6 (solar) and 2 $\times 10^{-5}$;
- the cosmic ray ionisation rate: 5×10^{-17} s^{-1} (assumed as our standard value) and 10 times higher.

Note that varying the C, O and N elemental abundances can be considered, coarsely, as mimicking, qualitatively, the degree of depletion of these elements onto the grain mantles. Furthermore, we varied the cosmic ray ionisation rate as this is a rather uncertain parameter that could be enhanced with respect to the "standard" value because of the presence of X-rays or an energetic ≥MeV particles source embedded inside the envelope (e.g. Doty et al. (2004); Ceccarelli et al. (2014b)).

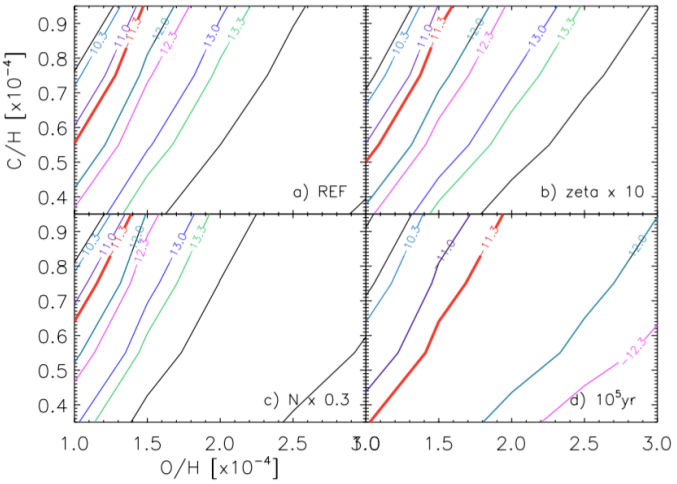

Fig. 6. Predicted HC_3N abundance (in log) as a function of the O/H (x-axis) and C/H (y-axis) for four cases: the reference model, described in the text (upper left panel), and then the same but with a cosmic rate ionisation increased by a factor ten (upper right panel), a nitrogen elemental abundance decreased by a factor three (lower left panel) and at a time of 10^5yr (lower right panel). The thick red lines mark the HC_3N abundance measured in the cold envelope of IRAS16293.

The results of the modelling are plotted in Figure 6. The top left panel is our reference model, with standard cosmic ray ionization rate (5×10^{-17} s^{-1}), at chemical equilibrium ($\geq 10^6$ yr), and with a solar abundance of nitrogen (6.2×10^{-5}). Note that the values of the HC_3N abundances are log of the fractional abundance with respect to the total number of hydrogen nuclei, hence the best match with the observations is for a value of -11.3. We find that this value is reached within our reference model for low values of O/H ($\leq 1.5\times10^{-4}$) and for a O/C ratio between 1.5 and 2, with the lowest O/C ratio needed with the highest O/H abundance. This implies that both oxygen and carbon are mostly frozen onto the grain icy mantles by about the same factor, as the O/C ratio is similar to the one in the Sun (1.8; see e.g. Asplund et al. (2009)) and in the HII regions (1.4; see e.g. García-Rojas & Esteban (2007)). Increasing the cosmic rays ionisation rate by a factor of ten changes little the above conclusions, having as an effect a slightly larger parameter space in O/H and O/C to reproduce the observed HC_3N abundance. On the contrary, decreasing N/H by a factor of three slightly diminishes the O/H and O/C parameter space. Finally, the largest O/H and O/C parameter space that reproduces the observed HC_3N abundance in the cold envelope of IRAS16293 is obtained by considering earlier times, 10^5 years (bottom right of Figure 6). This possibly implies that the gas in the envelope is at a similar age to that of the protostar.

5.2. Hot corino

As we move towards the centre of the protostar(s) a jump in the HC_3N abundance by roughly two orders of magnitude is observed at around $\sim$ 80 K. So the first question to answer is what this 80 K represents. According to the TPD (Temperature Programmed Desorption) experiments by Collings et al. (2004), and successive similar works, in general, the ice sublimation is a complex process and it does not occur at one single temperature but occurs in several steps. In the particular case of iced HC_3N, it is expected to have two sublimation peaks, at a dust temperature of about 80 and 100 K, respectively (see Viti et al. (2004) for details). The first one corresponds to the so-called *volcano* ice desorption, whereas the second one corresponds to the ice co-desorption, namely the whole ice sublimation. Therefore, our *measured* jump temperature of 80 K indicates that the most important sublimation is due to the volcano desorption, while the co-desorption injects back only a fraction of the frozen HC_3N. In addition, the 80 K jump also tells us that, whatever other process contributing to the formation of HC_3N at lower ($\leq$ 80 K) temperatures, has to be negligible. In other words, considering the reactions in the synthesis of HC_3N reported at the beginning of §5, the desorption of C-bearing iced species, like for example CH_4, has to provide a negligible contribution to the HC_3N abundance.

In order to understand what all this implies, we ran UCL_CHEM again, but this time we included freeze-out of the gas species in the cold phase, to simulate the cold and dense prestellar phase. We then allowed thermal evaporation of the icy mantles as a function of the species and temperature of the dust following the 'recipe' of Collings et al. (2004), in which the ice sublimation occurs in several steps (see (Viti et al. 2004) for the details). We find that the jump in the HC_3N abundance from 10^{-11} to 10^{-9} occurs only if thermal evaporation due to the volcano peak occurs quickly, on a timescale of $\leq 10^{3-4}$yr, implying that the increase of the dust temperature to $\sim$ 80 K must indeed also occur quickly, on a similar timescale. In addition, if frozen species containing C, like CO and CH_4, sublimate at earlier times, namely at colder temperatures, and remain in the gas for too long prior to the volcano explosion, then the HC_3N abundance reaches much too high abundances too quickly. In other words, the sublimation of those species must have occurred not much before the volcano sublimation, again on timescales of $\leq 10^3$ yr.

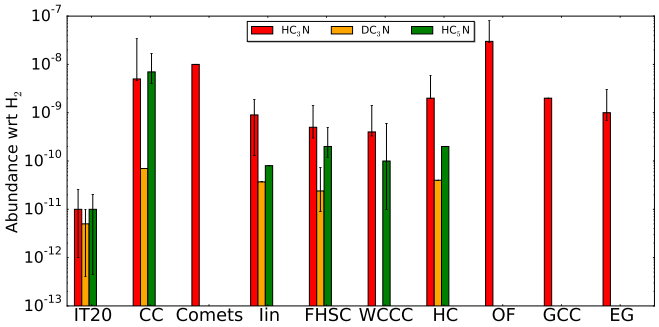

Fig. 7. Abundances of cyanopolynes in different sources: IRAS16293 outer envelope (IT20) and inner region (Iin) (this work), cold clouds (CC) (Winstanley & Nejad 1996; Miettinen 2014), comet Hale-Bopp at 1 AU assuming $H_2O/H_2=5\times10^{-5}$ (Comets) (Bockelée-Morvan et al. 2000), first hydrostatic core sources (FHSC) (Cordiner et al. 2012), Warm Carbon-Chain Chemistry sources (WCCC) (Sakai et al. 2008; Jørgensen et al. 2004), massive hot cores (HC) (Schöier et al. 2002; Esplugues et al. 2013), outflow sources (OF) (Bachiller & Pérez Gutiérrez 1997; Schöier et al. 2002), Galactic Center clouds (GCC) (Marr et al. 1993; Aladro et al. 2011), and external galaxies (EG) (Aladro et al. 2011).

5.3. HC_5N

We finally note that none of our models can reproduce an HC_5N abundance comparable to the one of HC_3N, as observed in the cold envelope of IRAS16293. All models predict indeed a much lower HC_5N abundance, by more than a factor ten, than the HC_3N abundance. Since in the warm (T$\geq$80 K) region we only derive an upper limit for the HC_5N abundance (which is at least ten times lower than the HC_3N one), the models can not be constrained. The failure of our models to reproduce HC_5N in the cold envelope is likely due to a lack of a comprehensive network for the formation and destruction of the species HC_5N and, therefore, calls for a revision of its gaseous chemistry.

6. Discussion

6.1. General remarks on cyanopolyynes in different environments

In the Introduction, we mentioned that cyanopolyynes are almost ubiquitous in the ISM. Here we compare the cyanopolyynes abundance derived in this work with that found in various galactic and extragalactic environments, which possess different conditions (temperature, density, and history). Fig. 7 graphically shows this comparison.

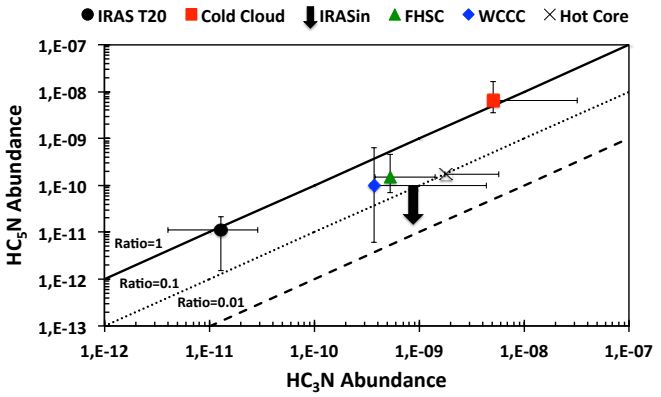

Fig. 8. Abundance of HC_5N as a function of the abundance of HC_3N in different protostellar and cold sources: inner (black arrow) and outer envelope (T_{20}) of IRAS16293 (black filled circle) presented in this work, Warm Carbon-Chain Chemistry (WCCC) sources (blue diamond) (Sakai et al. 2008; Jørgensen et al. 2004), First Hydrostatic Core (FHSC) source (green triangle) (Cordiner et al. 2012), Hot Cores sources (cross) (Schöier et al. 2002; Esplugues et al. 2013), and Galactic Center Clouds (red square) (Marr et al. 1993; Aladro et al. 2011).

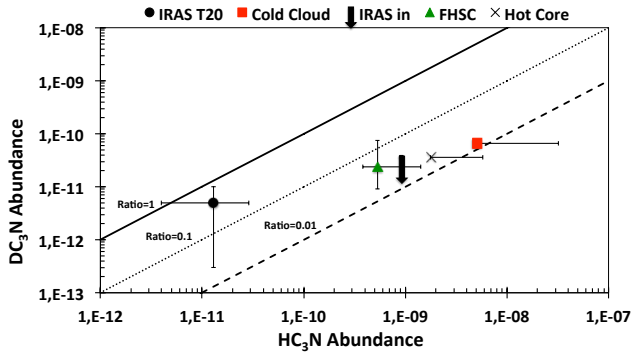

Fig. 9. Abundance of DC_3N as a function of the abundance of HC_3N in different protostellar and cold sources. The symbols are the same that those in Figure 8.

From this figure, we can remark the following: (i) HC_3N is present everywhere in the ISM with relatively high abundances; (ii) the abundance in the cold envelope of IRAS16293 is the lowest in the plot, implying a high degree of freezing of oxygen and carbon, as indeed suggested by the chemical model analysis; (iii) HC_3N and HC_5N have relatively similar abundances in the IRAS16293 outer envelope, Cold Cloud, First Hydrostatic Core (FHSC) and Warm Carbon-Chain Chemistry (WCCC) sources, namely in the cold objects of the figure, implying that the derived ratio $HC_5N/HC_3N \sim 1$ in IRAS16293 cold envelope is not, after all, a peculiarity, but likely due to the cold temperature; (iv) DC_3N is only detected in cold objects except in the warm envelope of IRAS16293 and the Hot Cores, suggesting that, in those sources, it is linked to the mantle sublimation, in a way or another, as, again, found by our chemical modelling.

6.2. The present and past history of IRAS16293

Our analysis of the TIMASSS spectral survey reveals the presence of HC_3N, HC_5N and DC_3N in IRAS16293. HC_3N was previously detected by van Dishoeck et al. (1993) and its abundance has been analysed by Schöier et al. (2002) with a two step abundance model, where the jump was assumed to occur at 90 K. Schöier et al. (2002) found $HC_3N/H_2 \sim 10^{-9}$ in the inner warm part and $\leq\sim 10^{-10}$ in the outer envelope. Note that they could not derive a value for the outer envelope, nor estimate where the jump occurs, because they only detected 3 lines. Nonetheless, their estimates are in excellent agreement with our new estimates (Table 3).

A very important point is that we not only could estimate the cold envelope abundance, but we were also able to determine where the jump occurs, an essential information for the determination of the origin of HC_3N in IRAS16293. Our chemical modeling (§ 5) shows that, in the cold envelope, the HC_3N abundance is reproduced for low values of oxygen and carbon in the gas phase, implying that these specis are heavily frozen onto the grain mantles. The O/C ratio is between 1.5 and 2, similar to the solar one, if the chemistry of the envelope is a fossil, namely built up during the $\sim 10^7$ yr life of the parental molecular cloud. If, on the contrary, the chemistry was reset (for whatever reason) and evolved in a shorter time, e.g. in 10^5 yr, the O/C ratio that reproduces the observations could be as high as 3, but the oxygen and carbon have, anyway, remained mostly frozen onto the grain mantles. Probably the most important point to remark is that the HC_3N abundance is very low, a very tiny fraction of the CO abundance, the major reservoir of the carbon, so that little variations in the CO abundance result in large ones in the HC_3N abundance.

A second extremely interesting point is that the HC_3N abundance undergoes a jump of about one hundred when the dust temperature reaches 80 K. These two values provide us with very strong constraints on how the collapse of IRAS16293 occurred: it must have occurred so fast that the sublimation of C-bearing ices, such as CO and methane, has not yet produced HC_3N in enough large abundances to 'mask' the jump due to the volcano sublimation of the ices at 80 K Collings et al. (2004); Viti et al. (2004). An approximate value of this time is $\sim 10^3$ yr, based on our modeling. In other words, the HC_3N measured abundance jump temperature and abundance in the warm envelope both suggest that IRAS16293 is a very young object, not surprisingly, and that the envelope dust heating took no more than $\sim 10^3$ yr to occur.

A third result from the present study is the large measured abundance of HC_5N, for the first time detected in a solar type protostar. It is indeed only ten times lower than HC_3N in the inner warm region and similar to the HC_3N abundance in the outer cold envelope. When compared to other protostellar sources where HC_5N has been detected, indeed, this ratio is not so anomalous. Figure 8 shows the two abundances in several protostellar sources and cold clouds. The two coldest sources have both an $HC_5N/HC_3N \sim 1$, while in the other sources this ratio is ~ 0.1. However, our chemical model fails to reproduce such a high abundance of HC_5N, despite including part of the most updated chemical network, recently revised by Loison et al. (2014). Evidently, we are missing key reactions that form this species.

6.3. The HC_3N deuteration

Finally, we detected, for the first time, the DC_3N in a solar type protostar. The deuteration of HC_3N is about 50% in the outer cold envelope and less than 5% in the warm part. This also provides us with important clues on the present and past history of IRAS16293. First, the high deuteration in the cold envelope tells us that this is, indeed, a present day product, namely it is caused by a cold and CO depleted gas, in agreement with previous observations and theoretical predictions (e.g. Ceccarelli et al. (2014a)).

The very low deuteration in the warm part is, on the contrary, more intriguing. Indeed, it cannot be the result of an initial high deuteration which has been diminished by gas phase reactions, because, as we have argued above, HC_3N is the result of the volcano sublimation which occurred because of a quick, $\leq 10^3$yr, heating of the dust. So it must be a fossil from the dust before the warming phase. Probably, this is one of the few very clear cases of fossil deuteration where there are no doubts that it is pristine (another one, to our knowledge, is the one of HDCO in the protostellar molecular shock L1157-B1; Fontani et al. (2014)). The deuteration in IRAS16293 is, in general, very high, with, for example, a doubly deuterated ratio of formaldehyde of $\sim 30\%$ (Ceccarelli et al. 1998) and a triply deuterated ratio of methanol of a few percent (Parise et al. 2004). While at present we still do not have a clear measure of the formaldehyde deuteration in the warmer and colder envelope separately (e.g. Ceccarelli et al. (2001)), methanol should be entirely concentrated in the warm region. However, recently, deuterated formamide has been reported in IRAS16293, measured from ALMA observations, which clearly show that formamide line emission is associated with the warm hot corino (Coutens et al. 2016). They measured a deuteration ratio of a few percent, actually similar to that found in HC_3N in the present work. So clearly the molecular deuteration is a complex phenomenon even within the same source.

If our reasoning above is correct, namely the present day gaseous HC_3N is the sublimation product of previously frozen HC_3N, then its relatively small deuteration tells us that this species is an "early" chemical product, namely it was formed in a time when the gas temperature was not too low and, mostly importantly, the CO was not depleted yet (see e.g. Ceccarelli et al. (2014a)). This is in perfect agreement, indeed, with the models of HC_3N formation, which show that HC_3N is *abundantly* formed *before* the full trapping of carbon into CO (e.g. Loison et al. (2014)). Therefore, the low DC_3N/HC_3N in the warm part is well explained by the picture that abundant HC_3N has been formed during the tenuous molecular cloud phase and then frozen onto the ice mantles when the condensation that gave birth to IRAS16293 increased in density while decreased in temperature. Then, we predict that the deuteration of HC_3N in the hot corino regions could be a good probe of the timescale of the collapse too. Of course, detailed modeling will be necessary to quantify this affirmation.

Meanwhile, the collection of previous measures of DC_3N/HC_3N, shown in Figure 9, provides support to our thesis. With the exception of the cold envelope of IRAS16293, all other sources where DC_3N has been observed, possess a HC_3N deuteration of a few percent, in agreement with the hypothesis that HC_3N is an early chemical product.

7. Conclusions

We detect several lines from cyanoacetylene (HC_3N) and cyanodiacetylene (HC_5N), and provide an upper limit to the abundance of cyanotriacetylene (HC_7N) and other undetected cyanopolyynes. Also, we report the first detection of deuterated cyanoacetylene, DC_3N, in a solar type protostar. On the contrary, we did not detect any ^{13}C cyanopolyyne isotopologue. We found that the HC_3N abundance is roughly constant($\sim 1.3 \times 10^{-11}$) in the outer cold envelope of IRAS16293-2422 and it increases, as a step-function, by about a factor 100 in the inner region where the dust temperature exceeds 80 K. The HC_5N has an abundance similar to HC_3N in the outer envelope and about a factor of ten lower in the inner region.

A comparison with a chemical model provides constraints on the oxygen and carbon gaseous abundance in the outer envelope and, most importantly, on the age of the source. The HC_3N abundance derived in the inner region and where the jump occurs also provide strong constraints on the time taken for the dust to warm up to 80 K, which has to be less than $\sim 10^3 - 10^4$ yr.

Finally, the cyanoacetylene deuteration is about 50% in the outer envelope and $\sim 5\%$ in the warm inner region. The relatively low deuteration in the warm region suggests that we are seeing an almost 'untouched' fossil of the HC_3N, abundantly formed in the tenuous phase of the pre-collapse and then frozen into the grain mantles at a later phase.

Acknowledgements. We wish to thank Alexander Faure for providing us with the HC_3N collisional coefficients before their publicaiton. This research was supported in part by the National Science Foundation under Grant No. NSF PHY11-25915. We acknowledge the financial support from the university of Al-Muthana and ministry of higher education and scientific research in Iraq. EM acknowledges support from the Brazilian agency FAPESP under the grants 2014/22095-6 and 2015/22254-0.

References

Aladro, R., Martín-Pintado, J., Martín, S., Mauersberger, R., & Bayet, E. 2011, A&A, 525, A89
Asplund, M., Grevesse, N., Sauval, A. J., & Scott, P. 2009, ARA&A, 47, 481
Bachiller, R. & Pérez Gutiérrez, M. 1997, ApJ, 487, L93
Bell, M. B., Feldman, P. A., Travers, M. J., et al. 1997, ApJ, 483, L61
Ben Abdallah, D., Najar, F., Jaidane, N., Dumouchel, F., & Lique, F. 2012, MNRAS, 419, 2441
Bockelée-Morvan, D., Lis, D. C., Wink, J. E., et al. 2000, A&A, 353, 1101
Brack, A. 1998, The Molecular Origins of Life: Assembling Pieces of the Puzzle (Cambridge University Press)
Caselli, P. & Ceccarelli, C. 2012, A&A Rev., 20, 56
Caselli, P., Walmsley, C. M., Terzieva, R., & Herbst, E. 1998, ApJ, 499, 234
Caux, E., Kahane, C., Castets, A., et al. 2011, A&A, 532, A23
Cazaux, S., Tielens, A. G. G. M., Ceccarelli, C., et al. 2003, ApJ, 593, L51
Ceccarelli, C., Caselli, P., Bockelée-Morvan, D., et al. 2014a, Protostars and Planets VI, 859
Ceccarelli, C., Castets, A., Caux, E., et al. 2000, A&A, 355, 1129
Ceccarelli, C., Castets, A., Loinard, L., Caux, E., & Tielens, A. G. G. M. 1998, A&A, 338, L43
Ceccarelli, C., Dominik, C., López-Sepulcre, A., et al. 2014b, ApJ, 790, L1
Ceccarelli, C., Hollenbach, D. J., & Tielens, A. G. G. M. 1996, ApJ, 471, 400
Ceccarelli, C., Loinard, L., Castets, A., et al. 2001, A&A, 372, 998
Ceccarelli, C., Maret, S., Tielens, A. G. G. M., Castets, A., & Caux, E. 2003, A&A, 410, 587
Cernicharo, J. & Guelin, M. 1996, A&A, 309, L27

Chandler, C. J., Brogan, C. L., Shirley, Y. L., & Loinard, L. 2005, ApJ, 632, 371
Clarke, D. W. & Ferris, J. P. 1995, Icarus, 115, 119
Collings, M. P., Anderson, M. A., Chen, R., et al. 2004, MNRAS, 354, 1133
Cordiner, M. A., Charnley, S. B., Wirström, E. S., & Smith, R. G. 2012, ApJ, 744, 131
Coutens, A., Jørgensen, J. K., van der Wiel, M. H. D., et al. 2016, A&A, 590, L6
Crimier, N., Ceccarelli, C., Maret, S., et al. 2010, A&A, 519, A65
Doty, S. D., Schöier, F. L., & van Dishoeck, E. F. 2004, A&A, 418, 1021
Esplugues, G. B., Cernicharo, J., Viti, S., et al. 2013, A&A, 559, A51
Faure, A., Lique, F., & Wiesenfeld, L. 2016, MNRAS, 460, 2103
Fontani, F., Codella, C., Ceccarelli, C., et al. 2014, ApJ, 788, L43
Friesen, R. K., Medeiros, L., Schnee, S., et al. 2013, MNRAS, 436, 1513
García-Rojas, J. & Esteban, C. 2007, ApJ, 670, 457
Goesmann, F., Rosenbauer, H., Bredehöft, J. H., et al. 2015, Science, 349 [http://science.sciencemag.org/content/349/6247/aab0689.full.pdf]
Jaber, A. A., Ceccarelli, C., Kahane, C., & Caux, E. 2014, ApJ, 791, 29
Jørgensen, J. K., Bourke, T. L., Nguyen Luong, Q., & Takakuwa, S. 2011, A&A, 534, A100
Jørgensen, J. K., Schöier, F. L., & van Dishoeck, E. F. 2004, A&A, 416, 603
Loinard, L., Torres, R. M., Mioduszewski, A. J., & Rodríguez, L. F. 2008, ApJ, 675, L29
Loinard, L., Zapata, L. A., Rodríguez, L. F., et al. 2013, MNRAS, 430, L10
Loison, J.-C., Wakelam, V., Hickson, K. M., Bergeat, A., & Mereau, R. 2014, MNRAS, 437, 930
Lunine. 2009, EPJ Web of Conferences, 1, 267
Marr, J. M., Wright, M. C. H., & Backer, D. C. 1993, ApJ, 411, 667
McElroy, D., Walsh, C., Markwick, A. J., et al. 2013, A&A, 550, A36
Miettinen, O. 2014, A&A, 562, A3
Mizuno, A., Fukui, Y., Iwata, T., Nozawa, S., & Takano, T. 1990, ApJ, 356, 184
Müller, H. S. P., Schlöder, F., Stutzki, J., & Winnewisser, G. 2005, Journal of Molecular Structure, 742, 215
Mundy, L. G., Wootten, A., Wilking, B. A., Blake, G. A., & Sargent, A. I. 1992, ApJ, 385, 306
Parise, B., Castets, A., Herbst, E., et al. 2004, A&A, 416, 159
Pickett, H. M., Poynter, R. L., Cohen, E. A., et al. 1998, J. Quant. Spectr. Rad. Transf., 60, 883
Pineda, J. E., Maury, A. J., Fuller, G. A., et al. 2012, A&A, 544, L7
Sakai, N., Sakai, T., Hirota, T., & Yamamoto, S. 2008, ApJ, 672, 371
Schöier, F. L., Jørgensen, J. K., van Dishoeck, E. F., & Blake, G. A. 2002, A&A, 390, 1001
Snell, R. L., Schloerb, F. P., Young, J. S., Hjalmarson, A., & Friberg, P. 1981, ApJ, 244, 45
Suzuki, H., Yamamoto, S., Ohishi, M., et al. 1992, ApJ, 392, 551
van Dishoeck, E. F., Blake, G. A., Draine, B. T., & Lunine, J. I. 1993, in Protostars and Planets III, ed. E. H. Levy & J. I. Lunine, 163–241
Viti, S., Collings, M. P., Dever, J. W., McCoustra, M. R. S., & Williams, D. A. 2004, MNRAS, 354, 1141
Wakelam, V., Loison, J.-C., Herbst, E., et al. 2015, ApJS, 217, 20
Wernli, M., Wiesenfeld, L., Faure, A., & Valiron, P. 2007, A&A, 464, 1147
Winstanley, N. & Nejad, L. A. M. 1996, Ap&SS, 240, 13
Wootten, A. 1989, ApJ, 337, 858
Zapata, L. A., Loinard, L., Rodríguez, L. F., et al. 2013, ApJ, 764, L14

Appendix A: Figures on the HC_3N modeling

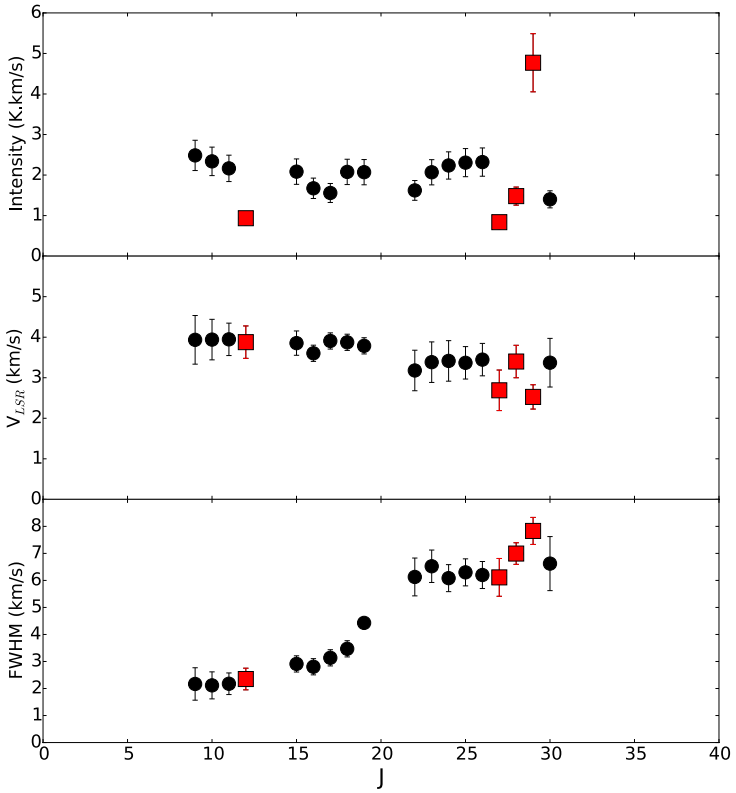

Fig. A.1. HC_3N line intensity (upper panel), rest velocity V_{LSR} (middle panel) and FWHM (bottom panel) as a function of the upper J of the transition. The red squares show the lines that have been discarded because they do not satisfy all criteria 3 to 5 of §3.2 (see text).

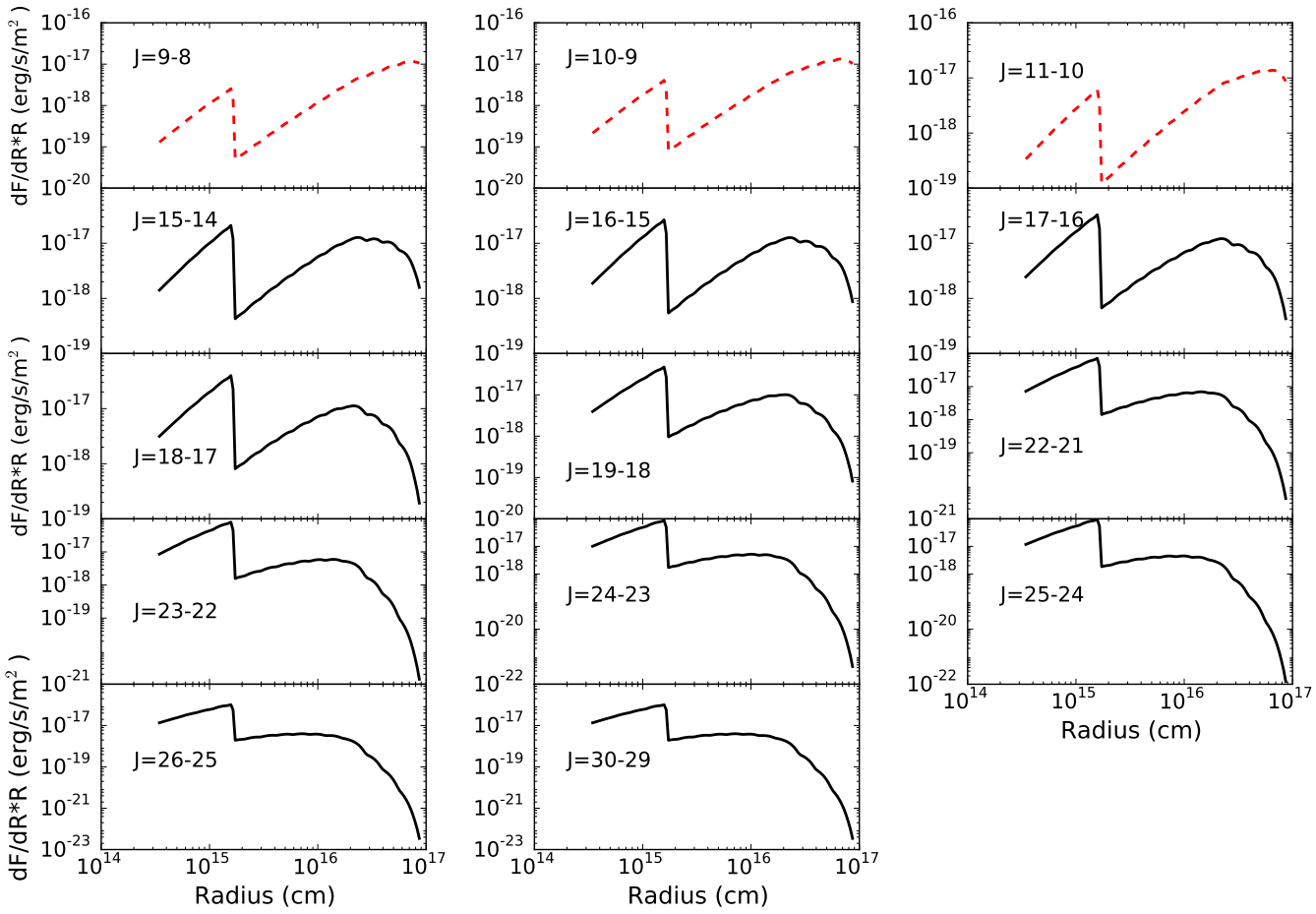

Fig. A.2. Predicted contribution to the integrated line intensity ($dF/dr * r$) of a shell at a radius r for the HC_3N lines. This model corresponds to α=0, T_{jump}=80 K, $X_{in} = 3.6 \times 10^{-10}$, and $X_{out} = 6.0 \times 10^{-11}$. The 3 upper red dashed curves show an increasing emission towards the maximum radius and very likely contaminated by the molecular cloud (see 4.2.1).

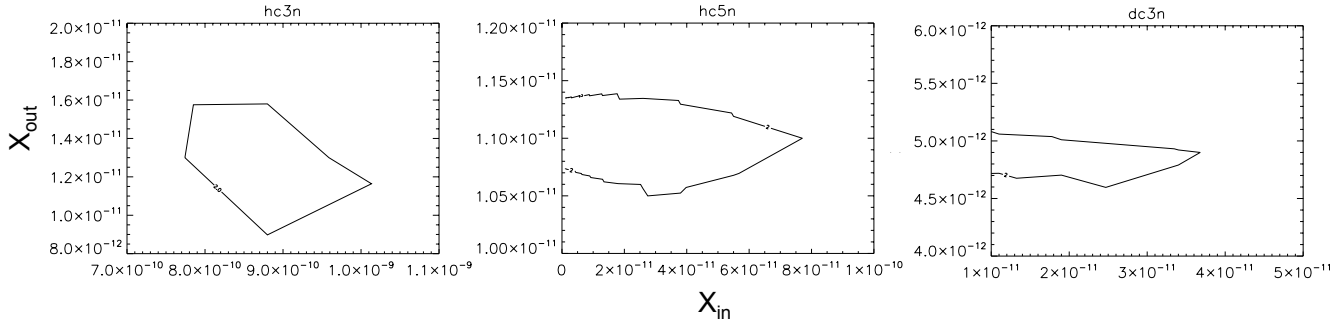

Fig. A.3. χ^2 contour plots for HC_3N (left), HC_5N (middle) and DC_3N (right) as a function of X_{in} and X_{out}. The predictions refer to a model with T_{jump}=80 K and α=0.

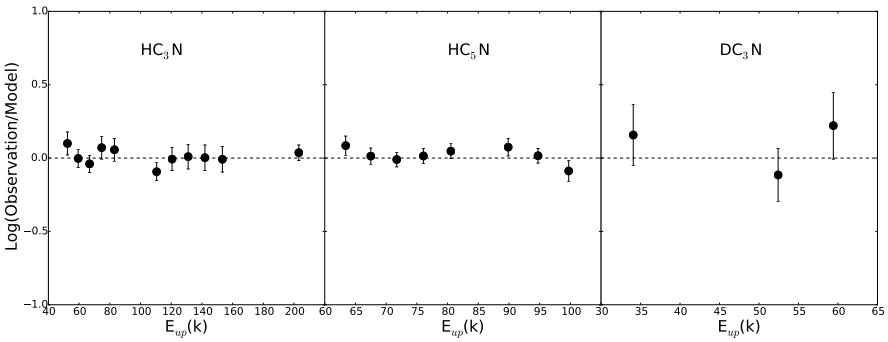

Fig. A.4. Ratio of the observed over predicted line flux as a function of the upper level energy of the transition for the model 2 (T_{jump}=80 K and α=0), for HC_3N (left), HC_5N (middle) and DC_3N (right), respectively.

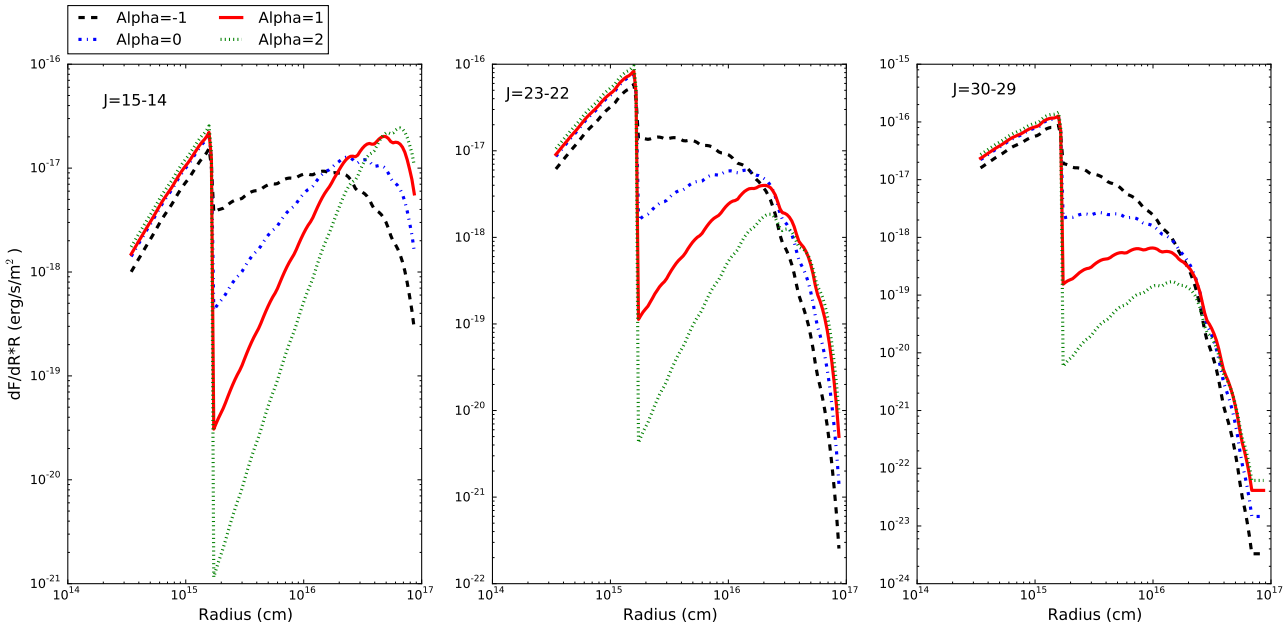

Fig. A.5. The velocity-integrated flux emitted from each shell at a radius r ($dF/dr * r$) as a function of the radius for the HC_3N four best NON-LTE model, for three low, middle and high value of J.